

Response of small sea ice floes in regular waves: a comparison of numerical and experimental results

Wei Bai^{1, 2, *}, Tong Zhang² and David J. McGovern³

1. School of Computing, Mathematics and Digital Technology, Manchester Metropolitan University, Chester Street,
Manchester M1 5GD, UK

2. Department of Civil and Environmental Engineering, National University of Singapore, Kent Ridge, Singapore 117576,
Singapore

3. Department of Civil, Environmental & Geomatic Engineering, University College London, Gower Street, London, WC1E
6BT, UK

Abstract

In severe seas ice floes can gain significant kinetic energy presenting a hazard to offshore structures and shipping. A numerical investigation is presented to investigate the kinematic response of sea ice floes in waves. The results are compared against available experimental data. The surge, heave and drift velocity are analysed for various different ice floe shapes using the potential flow model HydroSTAR[®] and the viscous flow CFD model OpenFOAM[®]. The results show relative wavelength (λ normalised with floe length L_c) λ/L_c strongly influences heave and surge, with a heave resonance occurring at $\lambda/L_c = 8$ for the cubic floe not being correspondingly observed for the square floe. The heave Response Amplitude Operator (RAO) is found to increase with floe thickness with a resonance occurring when relative thickness $b/L_c \geq 0.5$. Shape is observed to be less important than thickness. At small values of λ/L_c the floe is observed to move forward over the whole wavelength resulting in its drift displacement. Both vertical velocity relative to theoretical particle velocity V_y/V_p and ratio of forward and backward velocities show resonance at $\lambda/L_c = 8$. Comparing with experimental data, the linear analysis using HydroSTAR[®] overestimates the heave and surge RAOs. OpenFOAM[®], however, appears to provide a much better agreement with the experimental data indicating viscosity plays an important role in floe kinematics.

Key words: Ice floe; Dynamic response; Linear analysis; Computational fluid dynamics; Experimental study

* Corresponding author.
E-mail address: w.bai@hotmail.com (W. Bai).

30

31 **1. Introduction**

32

33 The trend in the decline of Arctic sea ice is predicted to lead to an ice-free Arctic Ocean by 2040 (ACIA,
34 2004). Such seasonal reduction in sea ice coverage may open the North West Passage and Northern Sea
35 Routes to shipping, greatly reducing the journey time between the Pacific and Atlantic Oceans. Additionally,
36 according to a USGS (United States Geological Survey) survey between 13 and 30% of the world's
37 untapped oil and gas are thought to be located beneath the Arctic Ocean (USGS, 2008). The reduction in ice
38 coverage is cause for increased interest in exploiting these reserves.

39 The Arctic is a particularly harsh environment and hazards to offshore and shipping operations include
40 that of sea ice interactions (Thompson and Rogers, 2014). The loss of ice coverage will increase fetch and, in
41 low concentrations, such as stretches of ocean adjacent to but not within the Marginal Ice Zone (MIZ),
42 motions of a sea ice floe (floating ice block which is not attached to land) that is small with respect the
43 dominant wavelength (λ) will be driven by ocean waves and become significant in severe seas. The analysis
44 of the problem is similar to that of a thin, free-floating body, and a detailed review is given in McGovern and
45 Bai (2014a). In the case of small fragments of sea ice, i.e., up to tens of meters in size and much smaller than
46 the dominant wavelengths, the floe is essentially non-compliant (Meylan and Squire, 1994, 1996, McGovern
47 and Bai, 2014a). In such a case flexural response of the floe is negligible and radiation damping is dominant.
48 The floes may still cover a large region of many kilometres in length, but will be found in all different sizes
49 down to small floes. Such small floes even in the MIZ are sensitive to full six degrees of freedom of motions
50 from wave forcings (Frankenstein et al., 2001). Indeed such motions have been measured in the field on
51 isolated glacial ice bergs of a variety of sizes (Wadhams et al., 1983). Understanding the kinematic response
52 of a small ice floe in wave is, therefore, key to properly addressing the potential hazard that such a floe may
53 have to offshore operations and shipping in the Arctic.

54 Due to its significance in cold regions engineering practice, there has been extensive research on drift
55 motions of small ice floes. Initially, researchers focused more on the derivation of theoretical or semi-
56 theoretical models to solve the simplified ice problems. For example, Rumer et al. (1979) extended the
57 Morison's equation to calculate the drift motion of small floating object in a gravity wave field. Shen and
58 Ackley (1991) used a one-dimensional model to study collisions between ice floes and herding using the

59 slope-sliding model proposed in Rumer et al. (1979). Shen and Zhong (2001) found that wave reflection has
60 a profound effect on the drift pattern. Even for a very small reflection coefficient, the floating object can stop
61 its propagation after some time. This trapping phenomenon depends on the added mass and drag coefficients.
62 Marchenko (1999) independently derived a similar slope-sliding theory as in Rumer et al. (1979).
63 Grotamaack & Meylan (2006) related the two theories in Marchenko (1999), Shen and Zhong (2001) and
64 identified an error in the derivation of Rumer et al. (1979). Recently, Huang et al. (2016) presented an
65 improved analytical solution to the drift of small rigid floating objects of arbitrary shapes under regular
66 waves.

67 Apart from the two comprehensive reviews in Squire et al. (1995) and Squire (2007) where a large
68 amount of research on the interaction of sea ice and ocean waves in the MIZ have been summarised, many
69 experiments and theoretical studies have been carried out to study the response of small floating objects in
70 waves. Arunachalam et al. (1987) analyzed the short term motion of icebergs in linear waves both
71 theoretically and experimentally. Lever et al. (1988a, 1988b) and Huang et al. (2011) studied different
72 factors which can affect the motion and drift velocity of small icebergs experimentally. However, it can be
73 seen that most attention has focused on glacial icebergs, which are now well understood. Attention,
74 including the works of Meylan and Squire (1994, 1996) and Meylan (2002), has focused on the flexural
75 response of thin floating bodies in waves. Of interest here is how the compliant properties of the floes affect
76 floe kinematic and reflection response.

77 More recently, Montiel et al. (2013a, 2013b) presented measurements of the oscillatory motions of thin
78 plastic disk in regular waves, and compared the measurements with predictions of the potential flow model.
79 Bennetts and Williams (2015) presented measured surge, heave and pitch motions of a solitary wooden disk
80 at a subset of the incident wave frequencies and amplitudes used for their tests. Their model was based on a
81 combined potential flow and thin plate theory, and the assumption of linear motions. Both a low-
82 concentration array in which discs were separated by approximately one disc diameter in equilibrium, and a
83 high-concentration array in which adjacent discs were almost touching in equilibrium, were considered in
84 their experiments. Meylan et al. (2015a) presented measurements of the surge, heave and pitch motions of a
85 thin plastic disk as a function of λ . They showed that the model predictions in their study are accurate for
86 incident λ approximately greater than two times floe diameter. Meylan et al. (2015b) tested the motions of

87 two different plate models with distinct material properties in regular waves by using the thin plate model.
88 The results indicated that the motions of floes are essentially linear.

89 In order to further understand kinematics of ice floes in water waves, McGovern and Bai (2014a)
90 conducted an experiment in a wave flume to investigate in detail the kinematic and dynamic response of ice
91 floes, their drift velocity, the influence of body geometry, thickness and other parameters. They concluded
92 that the ice floe's motion can be affected by its own properties such as shape and thickness and also the wave
93 properties such as wavelength. Additional discussion on ice floe interaction and impact characteristics with a
94 single fixed vertical cylinder was given in McGovern and Bai (2014b). They studied the effect of a single
95 cylinder on the upstream, near-cylinder, impact and post impact kinematics and velocities of floes of various
96 shapes in a variety of wave conditions. This paper is, therefore, the follow-up of our previous work on ice
97 floe kinematics. As the experimental data presented in McGovern and Bai (2014a) was not sufficiently
98 validated due to the lack of published data in the public domain, one aim of the present paper is to reproduce
99 the physical experiment numerically, so that the accuracy of both our experiment and the present numerical
100 study in the kinematics of ice floes can be firmly verified by the comprehensive comparison between the
101 numerical and experimental results. Also, different numerical tools are compared and recommendations are
102 made.

103 However, the literature review shows that CFD work on the kinematics of ice floes in water waves is very
104 rare. Therefore, identifying a suitable numerical tool for the ice floe problem is another aim of the present
105 paper. Two different numerical tools are chosen to carry out the numerical simulation: the linear analysis
106 based on the potential flow theory by the software HydroSTAR[®] and the computational fluid dynamic (CFD)
107 simulation based on the viscous flow theory by the open source tool OpenFOAM[®]. OpenFOAM[®], with the
108 advantage of being free and open source, has been adopted to solve many problems in coastal and offshore
109 engineering. In the study of Higuera et al. (2013), the OpenFOAM[®] was adopted to simulate several coastal
110 processes such as wave breaking and wave interaction with obstacle. Chen et al (2014) also used this CFD
111 tool to study wave interaction with a vertical cylinder. Both of these two studies indicated that the
112 OpenFOAM[®] is accurate and promising. After testing three validation cases, Morgan et al. (2010, 2011)
113 concluded that OpenFOAM[®] may potentially be a very useful tool for researchers and engineers in coastal
114 and offshore engineering. To simulate water waves, Jacobsen et al. (2012) extended OpenFOAM[®] with a
115 wave generation and absorption method. Furthermore, Higuera et al. (2013a, 2013b) implemented the

116 specific boundary conditions for realistic wave generations and presented a robust three-dimensional, two-
117 phase numerical model for practical applications in coastal engineering.

118

119 **2. Experimental study**

120

121 *2.1 Experiment setup*

122

123 The experimental set-up is described in detail in McGovern and Bai (2014a) and as such, is given here in
124 brief. The flume used is the 32 m long 2 m wide wave flume situated in the Hydraulic Engineering
125 Laboratory at the National University of Singapore. An effective absorption beach was located at the end of
126 the flume. Extensive testing during the construction of the flume showed that the beach reflects $< 5\%$ of
127 incident wave height, and this was confirmed by additional testing before the current experimental campaign
128 in McGovern and Bai (2014a). Sea ice models of various shapes are formed from paraffin wax (density $\rho =$
129 890 kg m^{-3}). The kinematic response of the models in regular waves is measured using a PhaseSpace Improv
130 motion tracking system, see Fig. 1a. This system tracks the full six-degrees-of-freedom of motion of the floe
131 models in the test section. Free surface elevation is recorded using four resistance-type wave gauges up and
132 downstream of the test section (Fig. 1b). The system consisted of 8 cameras mounted on a frame around the
133 test section supported by the flume walls. The cameras are able to resolve the LED to 0.1mm at a distance of
134 5m. The LEDs were positioned at equidistant points from each corner of the ice model. The system was
135 calibrated using a calibration wand on which LEDs are fixed at known distance apart. The accuracy of the
136 system is rated at 1% of the distance between the cameras and the measured LED (see McGovern and Bai,
137 2014a for more details).

138

139

140 Fig. 1 a) Image of a floe model with attached LED lights undergoing testing in regular waves and b) a schematic diagram of
141 the flume.

142

143 *2.2 Data processing*

144

145 Raw data obtained in the experiments is the time series record of displacement in the x and y directions.
146 The solid line in Fig. 2 shows the raw data of x displacement, which cannot be used directly for the analysis
147 of surge motion due to the presence of the drift motion. According to the engineering practice, the surge
148 motion refers to the periodically oscillating component in the x displacement. Therefore, to obtain the surge
149 motion the effect of drift motion should be separated from the time series record. It should be noted that due
150 to the different processing procedure, the surge motion defined in McGovern and Bai (2014a) is slightly
151 different to the conventional definition of surge motion widely adopted in engineering practice, since the
152 drift motion is not completely removed from the results of surge motion. Here, to be in line with the
153 conventional definition of surge motion, the mean value of x displacement at each time instant is calculated
154 by averaging the displacement around this time instant over one wave period. The oscillating surge motion is
155 eventually obtained by removing the mean at each time instant from the measured signal. By using this
156 processing procedure, the oscillating component can be separated from the motion in the x direction, as
157 shown by the dashed line in Fig. 2, which can be defined as the surge motion of moving body. The same
158 approach will also be adopted in the following sections to process the numerical results.

159

160

161 Fig. 2 An example of x displacement trace in experiment and corresponding surge motion after processing

162

163 In addition, since the large drift motion is a specific phenomenon associated with ice floes in waves, the
164 drift velocity is a key physical property that is of great engineering significance when studying ice impact
165 problems (Huang et al. 2011). Generally, the constant drift velocity in the quasi-steady state can be
166 computed by two approaches (Huang et al. 2011). One is to obtain the instantaneous mean velocity within
167 one wave period based on an up-crossing method that is widely used in analyzing irregular waves. In this
168 method, the period-averaged mean drift velocity is a function of time, and can be calculated by dividing the
169 horizontal displacement between two neighboring peaks by the wave period. The other method is to
170 calculate the mean drift velocity in the quasi-steady stage by determining the slope of a best-fitting linear
171 trend line, which is adopted in this study. For the purpose of demonstration, Fig. 3 shows the x displacement
172 trace for a typical case in the experiment, and the corresponding best-fitting linear trend line from 15s to 35s
173 marked by a thick solid line. The information regarding the performance of the approach is also shown in a

174 small table embedded in the figure. The drift velocity V_d can be easily determined by calculating the slope of
175 the best-fitting line. In the case shown in the figure, the drift velocity V_d is 0.05947m/s.

176

177

178 Fig. 3 An illustration of determination of drift velocity V_d using the best-fitting linear line approach.

179

180 3. Linear numerical analysis

181

182 There exist various numerical models ranging from the simplified linear potential flow model to the more
183 complete computational fluid dynamic simulations, which are available for the numerical simulation of
184 response of ice floes in water waves. However, each numerical model has its own advantages and
185 disadvantages due to various assumptions made and inherent natures of the model. In this study, we mainly
186 focus on two popular numerical models, and evaluate the performance of these two models.

187

188 3.1 Linear diffraction/radiation method

189

190 The fluid is assumed to be incompressible and inviscid, and the motion irrotational. The water wave
191 problem can be formulated in terms of a velocity potential $\phi(x, y, z, t)$, which satisfies Laplace's equation
192 within the fluid domain surrounding the ice floe (Chen et al. 2015),

$$193 \quad \nabla^2 \phi = 0, \quad (1)$$

194 and is subject to the boundary conditions applied on the ice floe surfaces given as:

$$195 \quad \frac{\partial \phi}{\partial n} = \mathbf{V}_n, \quad (2)$$

196 where n is the normal unit vector pointing out of the fluid domain, and \mathbf{V}_n the normal velocity component of
197 the solid surfaces. On the water surface, the first order boundary condition is

$$198 \quad \frac{\partial^2 \phi}{\partial t^2} + g \frac{\partial \phi}{\partial z} = 0, \quad (3)$$

199 where g is the acceleration due to gravity. In addition, a suitable radiation condition on the outer boundary
200 should be imposed to avoid the wave reflection from the far-field boundary.

201 This boundary value problem has been successfully solved in many widely used commercial software
202 packages. In this study, the software package HydroSTAR[®] is adopted, which provides a complete solution
203 of the first order problem of wave diffraction and radiation. The main output includes the wave forces and
204 moments, wave elevation and dynamic response of floating bodies. As for the problem of ice floes in water
205 waves investigated in the present study, this linear analysis tool is applied to simulate a cube of length 20cm,
206 and a square plate of length 30cm and thickness 5cm, in order to examine the capability of the linear analysis
207 for this thin ice floe problem. The assumption of $kL_c = O(1)$ is applicable for the potential flow model, where
208 k is the wave number and L_c is the typical body length. After the mesh convergence test, the numbers of
209 panels in the x , y and z directions are chosen to be 8, 8 and 8 for the cube in the calculation, while the
210 numbers of panels for the square plate are 18, 18 and 6. Due to the symmetry of the computational domain,
211 only a quarter of the body is considered in the calculation, so that there are in total 80 and 189 panels on the
212 cube and square plate surfaces, respectively.

213

214 *3.2 Numerical results and discussions*

215

216 Our experimental results reveal that ice floe kinematics can be affected by incident wave height H and
217 wavelength λ . However, in the linear analysis RAO (Response Amplitude Operator) of bodies is independent
218 with incident wave height. We, therefore, can only study the influence of wavelength on the dynamic
219 response of ice floes in waves. To make a direct comparison with our experiments, the wavelength is varied
220 from 1.0m to 3.0m for the cube and from 0.6m to 3.0m for the square plate, as in the experiments. The linear
221 analysis can directly provide the surge and heave RAOs, where the effect of drift is excluded. The numerical
222 results are compared with the experimental data measured at the wave steepness H/λ of 0.02 for the cube and
223 0.044 for the square plate, as shown in Fig. 4 and Fig. 5 respectively. From the comparison of surge and
224 heave RAOs of the cube as a function of relative wavelength λ/L_c , it can be seen that the surge RAO is in
225 acceptable agreement, but the numerical simulation over-predicts the heave response by four times that of
226 the experimental measurement at the peak frequency around $\lambda/L_c = 7 - 9$. Here, L_c is defined as the length of
227 the edge in horizontal plane for the square plate and the length of the edge for the cube respectively. For the
228 square plate in Fig. 5, the numerical results reveal that the linear analysis seems to over-predict both the
229 surge and heave RAOs. An unreasonable peak appears in both the surge and heave RAOs at about $\lambda/L_c = 3$,

230 whose value exceeds 1. Therefore, in the regime where λ/L_c is between 2 to 4, the linear analysis can be
231 considered to provide inaccurate results for the square plate considered here.

232

233

234 Fig. 4 Comparison of surge (a) and heave (b) RAOs of cube between the linear analysis and experiment

235

236 Fig. 5 Comparison of surge (a) and heave (b) RAOs of square plate between the linear analysis and experiment

237

238 Generally speaking, although with the similar trend, the linear analysis by HydroSTAR[®] is not able to
239 provide good agreement with the experimental results, especially in the resonance range for the heave
240 motion of the cube. The over-prediction of the numerical simulation is mainly due to the neglect of fluid
241 viscosity in the potential flow model, which is verified later in Figs. 9 and 10 by the numerical results
242 obtained using the viscous flow solver OpenFOAM[®] where the viscosity of fluid is considered. It is
243 unsurprising that the results obtained by the linear potential flow analysis cannot agree with the experimental
244 results well, as it is known that this theory is only valid for certain range of body size relative to wavelength.
245 The only damping in the potential flow model is due to radiation damping, while as in the experimental case,
246 viscous damping appears to play a more significant role in accurately predicting the dynamic responses. In
247 addition to the assumptions made in the potential flow model, the linearization might be another source of
248 error in the linear analysis. At the same time, as the commercial software HydroSTAR[®] can only provide the
249 results in the frequency domain, which means the information about the displacement trace and the drift
250 velocity that are the significant physical properties when studying ice floes in water waves, is missing. The
251 advantage of the linear analysis is efficiency; the simulation can finish in a very short period of time. For a
252 particular case, full RAO can be obtained on a normal workstation in 10 minutes when 500 wave frequencies
253 are considered. However, to obtain more accurate numerical results with detailed information, a
254 computational fluid dynamic simulation with the nonlinearity and fluid viscosity being taken into account is
255 necessary.

256

257 **4. Computational fluid dynamic (CFD) simulation**

258

259 4.1 Mathematical formulation

260

261 The governing equations for viscous flows are the Reynolds averaged Navier-Stokes equations (Ferziger
262 and Peric, 2012) within the domain surrounding the ice floe:

$$263 \quad \frac{\partial \rho}{\partial t} + \frac{\partial}{\partial x_j} (\rho u_j) = 0, \quad (4)$$

$$264 \quad \frac{\partial}{\partial t} (\rho u_i) + \frac{\partial}{\partial x_j} (\rho u_j u_i) = -\frac{\partial p}{\partial x_i} + \frac{\partial}{\partial x_j} \left[\mu_e \left(\frac{\partial u_j}{\partial x_i} + \frac{\partial u_i}{\partial x_j} \right) \right] + \rho g_i, \quad (5)$$

265 where x_j ($j = 1, 2, 3$) represents the coordinate components, u_j is the fluid velocity, p is the pressure, ρ is the
266 fluid density. $\mu_e = \mu + \mu_f$, where μ is the fluid viscosity and μ_f is the turbulent eddy viscosity. In order to
267 close the above governing equations, the two-equation k - ε turbulence model is adopted to simulate the
268 turbulent flows:

$$269 \quad \frac{\partial}{\partial t} (\rho k) + \frac{\partial}{\partial x_j} (\rho u_j k) = \frac{\partial}{\partial x_j} \left[\left(\mu + \frac{\mu_f}{\delta_k} \right) \frac{\partial k}{\partial x_j} \right] + P_k - \rho \varepsilon, \quad (6)$$

$$270 \quad \frac{\partial}{\partial t} (\rho \varepsilon) + \frac{\partial}{\partial x_j} (\rho u_j \varepsilon) = \frac{\partial}{\partial x_j} \left[\left(\mu + \frac{\mu_f}{\delta_\varepsilon} \right) \frac{\partial \varepsilon}{\partial x_j} \right] + C_1 P_k \frac{\varepsilon}{k} - \rho C_2 \frac{\varepsilon^2}{k}, \quad (7)$$

$$271 \quad P_k = \mu_f \left(\frac{\partial u_j}{\partial x_i} + \frac{\partial u_i}{\partial x_j} \right) \frac{\partial u_i}{\partial x_j}, \quad (8)$$

272 where $\mu_f = C_\mu \rho k^2 / \varepsilon$, k is the turbulent kinetic energy, ε is the turbulent energy dissipation rate, δ_k and δ_ε are
273 the turbulent Schmidt numbers. The constants in the turbulence model are set as $C_\mu = 0.09$, $C_1 = 1.44$, $C_2 =$
274 1.92 , $\delta_k = 1.0$ and $\delta_\varepsilon = 1.33$.

275 Volume of Fluid method (VOF) (Hirt and Nichols, 1981) is adopted to capture the air-water interface (the
276 free water surface). In this method, the fraction of water volume existing in each computational element
277 (known as the volume fraction) is advected by solving the following transport equation:

$$278 \quad \frac{\partial \alpha}{\partial t} + \frac{\partial}{\partial x_j} (u_j \alpha) = 0, \quad (9)$$

279 where α is the volume fraction of water. The volume fraction is used as the weighting factor to predict the
280 fluid properties in each computational element,

281
$$\rho = \alpha\rho_w + (1-\alpha)\rho_a, \quad (10)$$

282
$$\mu = \alpha\mu_w + (1-\alpha)\mu_a, \quad (11)$$

283 where the subscripts w and a represent the corresponding fluid property of water and air respectively. It
284 should be noted that on the body surface, the non-slip boundary condition is applied.

285

286 *4.2 Numerical implementation of OpenFOAM®*

287

288 The CFD calculations are carried out using an open source CFD software, OpenFOAM® (Open Source
289 Field Operation and Manipulation) which was first released in 2004. OpenFOAM® is essentially a C++
290 library that is used to create solvers for various fluid flow problems. OpenFOAM® comes with a great
291 number of solvers but its open source nature can also enable users write their own solvers. Jacobsen et al.
292 (2012) developed a solver, called Waves2Foam, to deal with the wave generation and wave-structure
293 interaction problems. While this solver doesn't include the dynamic mesh utility in OpenFOAM® and as a
294 result cannot deal with floating bodies. In the present study, Waves2Foam is coupled with the dynamic mesh
295 function embedded in another OpenFOAM® solver, called WaveDyMFoam, such that the moving body
296 problems can be solved in the frame of Waves2Foam.

297 Three different types of floes are considered in the CFD calculations using OpenFOAM®: the first two are
298 the cube and square plate that have been defined before in the linear analysis, and the last geometry is a
299 regular triangle plate of length 30cm and thickness 5cm. The present study mainly investigates the effect of
300 wavelength on ice floe kinematics, by varying the wavelength from about 0.6m to 3.0m for all these three
301 geometries. In the simulation of the cube, the wave steepness is set to $H/\lambda = 0.02$, as used in the experiments.
302 However, the wave steepness H/λ remains to be 0.044 for both the square and triangle plates, which was also
303 adopted in the experiments for the same geometries. Various wave heights are also tested for the square plate
304 with the same wavelength to study the influence on the drift velocity. The effect of ice floe thickness is also
305 studied by a series tests for the square plate. Therefore, in total 54 test cases are run using OpenFOAM®.

306 In the numerical simulations, BlockMesh, a mesh type in OpenFOAM® which is very suitable for regular
307 geometries, is used to discretize the computational domain for the cube and square plate, where the total
308 numbers of elements are 400,000 and 432,000 respectively. For the triangle plate, because of the relatively

309 irregular shape of the body SnappyHexMesh, another mesh type in OpenFOAM® which is more robust for
310 irregular geometries, is used and 571,802 elements are adopted in the simulations. It should be noted that a
311 coarser mesh of 200,000 elements and a finer mesh of 800,000 elements have also been tested for the cube to
312 validate the feature of mesh convergence (not shown here). The calculations at those three meshes reveal that
313 the intermediate mesh of 400,000 elements and the finer mesh can provide very agreeable results that deviate
314 from those obtained at the coarser mesh, indicating that the results presented below at the adopted mesh is
315 convergent in terms of computational mesh. In addition, non-uniform mesh is used for all the three
316 geometries with suitable mesh refinement around the free surface and body surface. With 400,000 elements,
317 one simulation for a duration of 30s and a particular λ/L_c takes about 3 to 4 hours in OpenFOAM® using 8
318 computer processors. In this study, our main focus is on the global dynamic motion of bodies in waves,
319 rather than the detailed turbulent flow structures. Therefore, no special consideration has been given to the
320 treatment of flow boundary layer. In Fig. 6, an example mesh is shown for a floating square plate generated
321 in OpenFOAM®. Table 1 shows the wave properties and model shapes of simulations in OpenFOAM®.

322

323

324 Fig. 6 The example mesh in OpenFOAM® for ice floe problem

325

326 Table 1 Summary of OpenFOAM® simulations

327

328

329 **5. CFD and experimental Results**

330

331 *5.1 Time series of response*

332

333 Time series of body response is a direct output in both the numerical simulation and experimental
334 measurement. Fig. 7 shows the displacements in the x and y directions and the comparison between the
335 numerical results and experimental data for the square plate over five wave periods after the steady state has
336 been achieved. The steady state means both the surge and heave motions become periodic with constant
337 amplitudes and the drift component becomes a fixed value in each wave period. In this case, the wavelength

338 $\lambda = 3\text{m}$ and wave height $H = 0.132\text{m}$ are considered. As shown in the figure, the ice floe experiences a
339 periodic motion around the free surface in the y direction, whereas a clear drift can be observed although it
340 also moves forwards and backwards periodically in the x direction. The comparison between the numerical
341 results and experimental data shows that good agreement can be obtained for the surge and heave motions.
342 To better demonstrate the body motion, the trajectory of the square plate moving in waves is shown in Fig. 8,
343 from which we can see that the trajectory exhibits like a helix line rather than a closed line. The x
344 displacement is periodic, but also involves a drifting component.

345

346

347 Fig. 7 Numerical and experimental results of time series of x (a) and y (b) displacements for the square plate

348

349 Fig. 8 Numerical result of trajectory of the square plate in waves

350

351 5.2 Effect of wavelength

352

353 In the tests of Lever et al. (1988a) for the iceberg motions, it was concluded that wavelength λ is a
354 significant factor to influence the iceberg motions. In their experiments, four model geometries were adopted
355 to study the effect of geometry on dynamic responses of icebergs. For a particular geometry, the influence of
356 wavelength on body motions was also investigated. The results demonstrated that cylinder and cube models
357 show a peak in the heave RAO at $\lambda/L_c = 6$ and then tend to be around 1 at larger λ/L_c , while the sphere and
358 trapezoid show no peak. In this study, we first present our numerical and experimental results of surge and
359 heave RAOs for the cube and compare with the experimental data in Lever et al. (1988a), as shown in Fig. 9,
360 to validate both our numerical model and experiment. For the 20cm cubic model, in McGovern and Bai
361 (2014a) the test case was repeated for 6 times at each wave condition. The error bars of the experimental
362 data are shown in Fig. 9, from which we can see that the errors of the experiments are small (less than 8%).
363 We can also see from the figure that the surge and heave RAOs show different trend with the increase of
364 relative wavelength λ/L_c for the cube. The surge RAO shows a constant increase with the wavelength, and
365 after $\lambda/L_c = 10$ it approaches to 1, indicating the particle-like behavior of the ice floe. A peak appears in the
366 heave RAO at around $\lambda/L_c = 8$; the heave motion decreases and tends to approach to 1 while increasing the

367 wavelength so that the cube behaves like a water particle, in both the numerical, present and Lever et al.'s
 368 experimental results. Schwerdtfeger (1980) used a rectangular iceberg and assumed the motion only in the
 369 vertical cross-section. The frequencies of both linear and angular oscillations of a floating iceberg in the
 370 vertical plane were shown to converge to a certain value with the increase of body size in the horizontal
 371 plane. It was found that the heave resonance of an iceberg with straight sides can be easily computed by
 372 assuming linear oscillations:

$$373 \quad \left(\frac{\lambda}{h} \right)_{res} = 2\pi \frac{\rho_i}{\rho_w} (1 + m_c), \quad (12)$$

374 where h is the thickness of the iceberg, m_c is the added mass coefficient in heave, ρ_i and ρ_w are the densities
 375 of ice and water respectively. The added mass coefficient for the cube in this case can be determined
 376 approximately by the formula $ma = 0.7\rho a^3$, as shown in Levins and Plunkett (1980). With this added mass
 377 coefficient, Eq. (12) shows that the heave resonance occurs at $\lambda/L_c = 9.7$ for the ice cube, which agrees with
 378 the numerical and experimental results shown in Fig. 9. This probably can also explain the lack of resonance
 379 in the heave for the square plate, as shown later. Eq. (12), at the same time, demonstrates that the thickness
 380 of the ice might be another important parameter, which will be further discussed later in detail.

381

382

383 Fig. 9 Comparison of surge (a) and heave (b) RAOs of the cube between the present numerical and experimental results,
 384 and the experimental data in Lever et al. (1988a)

385

386 Further observation of Fig. 9 reveals that the numerical result of surge motion is slightly different from
 387 the present experimental data, but closer to the data in Lever et al. (1988a). On the other hand, the heave
 388 motion in the numerical simulation experiences a larger peak compared to the experimental results, which
 389 may be due to the other damping influences (such as the surface roughness of the ice floe and the tank walls)
 390 in the experiments that cannot be taken into account in the numerical simulations. However, in general the
 391 present numerical simulation is able to provide accurate surge and heave RAOs, and the present
 392 experimental results are also in good agreement with numerical and Lever et al.'s experimental results.

393 Fig. 10 shows the surge and heave RAOs of the square plate in the present numerical simulation and
 394 physical experiment both with the wave steepness of $H/\lambda = 0.044$. As seen in the figure, it is distinguishable

395 from the cube case that there is no obvious peak observed in the heave RAO, but the surge RAO shows the
396 similar characteristics with the cube case. It seems that the thickness of ice floe can affect the occurrence of
397 the resonance phenomenon in the heave motion, which will be further discussed later. A small discrepancy
398 can still be observed for $\lambda/L_c < 3$ in both heave and surge RAOs, which may be attributed to the small wave
399 height (about 2 cm) adopted in both the numerical and experimental studies. The wave height is small in
400 order to retain a constant wave steepness for these short waves. This may cause errors in both the
401 experiments and numerical simulations.

402

403

404 Fig. 10 Comparison of surge (a) and heave (b) RAOs of the square plate between the present numerical and experimental
405 results

406

407 Furthermore, with considering the over-prediction and unrealistic peak in the linear analysis, as shown in
408 Figs. 4 and 5, the CFD simulations can obtain much better results than the linear analysis, which is reflected
409 by the better agreement with the experimental data, especially for the cube case. As discussed before, the
410 over-prediction in the linear analysis is due to the linear nature and the omission of the fluid viscosity in the
411 basic assumptions of the linear potential flow model. Therefore, compared to the CFD simulation, the linear
412 analysis may not be very suitable in accurately modeling the motion of floating ice floes, even though it is
413 very efficient in computer time.

414

415 At the same time, the physical experiment also observes the phenomenon of green water appeared when
416 $\lambda/L_c < 5$ for the square plate. Green water is a quantity of water on the topside surface of body as a result of
417 wave actions. The same green water is also noticed in the numerical simulations, whereas the critical value
418 for the occurrence of this phenomenon is found to be around $\lambda/L_c = 4$. Fig. 11 shows the test cases with and
419 without the green water observed at $\lambda/L_c = 4$ and $\lambda/L_c = 10$ respectively for the square plate at the wave
420 steepness $H/\lambda = 0.044$. This green water effect may be one of the reasons for smaller surge and heave
421 motions at smaller wavelengths. This phenomenon agrees with the findings in Skene et al (2015), where a
422 theoretical model of overwash of a floating plate was presented and validated by laboratory experiments.
423 They also showed that overwash generally occurs for waves with relatively short lengths. For the cases with

424 $\lambda/L_c < 4$, the relative error of the numerical simulation is larger and the reason has been discussed. For the
425 cases with $\lambda/L_c > 4$, the relative error is less than 10% which means that the numerical results are reliable.

426

427

428 Fig. 11 The 3D free surface profile around the square plate for $\lambda/L_c = 4$ (a) with green water and $\lambda/L_c = 10$ (b) without green
429 water

430

431 5.3 Effect of model shape

432

433 In the physical experiments, a series of ice floes with different shapes have been tested. In the CFD
434 simulations, three model shapes are chosen to test the hydrodynamic performance of different bodies. For the
435 influence of other body shapes, see McGovern and Bai (2014) for more details. The three body shapes
436 chosen include the cube, square plate and triangle plate with streamline normal to one edge of the triangle.
437 Fig. 12 shows the surge and heave RAOs of different body shapes obtained by both the numerical
438 simulations and experiments. As seen in the figure, the surge motion presents an increasing trend with the
439 increase of wavelength for all the three body shapes, and the numerical results are in good agreement with
440 the experimental results. While for the heave RAO, results for different body shapes show great difference.
441 For the cube, both the numerical and experimental results show a peak approximately at $\lambda/L_c = 8$, where the
442 heave response can reach more than two times that of the wave height H . For the square and triangle plates,
443 there is no obvious heave resonance. Generally, for all the three body shapes, the numerical results show the
444 same trend with the experimental data. However, the numerical results seem to underestimate the heave
445 RAO for both the square and triangle plates when the wavelength is small. For the cases with $\lambda/L_c < 4$, the
446 relative errors of heave RAOs are relatively large especially for the cube and square plate. While for the
447 cases with $\lambda/L_c > 4$, the relative errors of all the three models are less than 10% except for the cube with λ/L_c
448 = 8. As for surge RAO, also the cube model shows the largest relative errors while the errors of all the three
449 models are in a reasonable range.

450

451

452 Fig. 12 Comparison of surge (a) and heave (b) RAOs of three different body shapes between the present numerical and
 453 experimental results

454

455 5.4 Ice floe velocity

456

457 The velocity of ice floe is an important parameter when calculating ice impact force on structures by using
 458 the Morison equation (Wong and Sego, 1989). In the numerical simulation, the velocity of floating body can
 459 be exported directly, while in the physical experiment the velocity can be calculated from the time series of
 460 body displacement. Fig. 13 shows a comparison of time series of velocities in the x and y directions between
 461 the numerical and experimental results for the square plate with the wavelength $\lambda = 3\text{m}$ and wave height $H =$
 462 0.132m . It can be seen that the x velocity in the positive x direction is obviously larger than that in the
 463 negative direction, which indicates the occurrence of the body drift in the x direction. For the heave velocity,
 464 the maximum upward and downward velocities are approximately the same. When the steady state is
 465 reached, the maximum x and y velocities of the square plate predicted by the numerical simulation agree
 466 reasonably well with the experimental results.

467

468

469 Fig. 13 Time series of x (a) and y (b) velocities obtained by both the numerical simulation and experiment for the square
 470 plate with $\lambda = 3\text{m}$ and $H = 0.132\text{m}$

471

472 Fig. 14 shows the x and y velocities, V_x and V_y , of the cube normalized by the corresponding theoretical
 473 water particle velocity V_p as a function of the relative wavelength λ/L_c . Here, V_x and V_y refer to the maximum
 474 velocities in the x and y directions respectively, and V_p is defined as:

$$475 \quad V_{px} = \frac{H}{2} \sigma \frac{\cosh k(h+z)}{\sinh kh} \cos(kx - \sigma t) \quad (13)$$

$$476 \quad V_{py} = \frac{H}{2} \sigma \frac{\sinh k(h+z)}{\sinh kh} \cos(kx - \sigma t) \quad (14)$$

477 As shown in the figure, the horizontal relative velocity V_x/V_p varies around 1 but shows no specific trend.

478 The vertical relative velocity V_y/V_p demonstrates the same trend as in the heave RAO with a resonance

479 happened at approximately $\lambda/L_c = 8$. As for comparison, the numerical results agree with the experimental
480 results well in V_y/V_p . However, V_x/V_p is smaller than the experimental results but with a similar trend.
481 Furthermore, with the increase of λ/L_c the ratio of the horizontal positive and negative velocities is also
482 shown in Fig. 15. As can be seen in the figure, the general trends of the numerical simulation and experiment
483 are the same. The ratio shows a peak at $\lambda/L_c = 8$ and with the increase of λ/L_c , the ratio approaches an
484 asymptotic value of 1.5.

485

486

487 Fig. 14 Comparison of numerical and experimental results of x (a) and y (b) velocities normalized by the theoretical water
488 particle velocity for the cube

489

490 Fig. 15 Comparison of numerical and experimental results of the ratio of horizontal positive and negative velocities for the
491 cube as a function of relative wavelength

492

493 For the cube, there is always a horizontal negative velocity at all the relative wavelengths investigated,
494 which indicates that the cube moves forwards and backwards. However, for the square plate, the physical
495 experiment shows that the horizontal negative velocity does not appear at small wavelengths when $\lambda/L_c < 5.3$.
496 In this situation, the floe keeps moving forwards all the time without any backward motion. The same
497 phenomenon is also observed in the present numerical simulation when $\lambda/L_c < 4$. This is because drift
498 velocity becomes dominant when λ/L_c is small. Fig. 16 shows the numerical results of surge displacement for
499 the square plate at $\lambda/L_c = 2$ and 5. With constant wave steepness, the larger wavelength implies that a higher
500 wave was used in the simulation. Without the obvious backward velocity, the floe moves even faster at λ/L_c
501 = 2 with a smaller wave height compared to that at $\lambda/L_c = 5$. This indicates that the drift velocity V_d does not
502 necessarily increase with the wave height, but is affected more by the relative wavelength.

503

504

505 Fig. 16 Numerical result of displacement in the x direction for the square plate at $\lambda/L_c = 2$ and 5

506

507 To visualize the velocity in the domain, Fig. 17 shows the velocity field around the cube with the relative
508 wavelength $\lambda/L_c = 13$ and wave height $H = 0.052\text{m}$ at two time instants. In Fig. 17(a), the wave crest passes
509 the cube at $t = 10.3\text{s}$, while the wave trough passes the cube at $t = 10.9\text{s}$ in Fig. 17(b). When the wave crest
510 passes, the velocity of most water particles around the body is pointing upwards and forwards so that the
511 body also moves in that direction. However, when the wave trough passes, the velocity of most particles
512 around the body is in the opposite direction, the body therefore moves downwards and backwards.

513
514
515 Figure. 17 Velocity field around the cube with $\lambda/L_c = 13$ and $H = 0.052\text{m}$ at two time instants: (a) $t = 10.3\text{s}$ and (b) $t = 10.9\text{s}$

517 5.5 Drift velocity

518 For a pure wave motion in fluid dynamics, the Stokes drift velocity is the average velocity when
519 following a specific fluid parcel as it travels with the fluid flow. In the Lagrangian description, fluid parcels
520 may drift far from their initial positions. The equation of the drift velocity is given as follow:

$$521 \quad V_d = \frac{ga^2k^2 \cosh 2k(h+z)}{\omega \sinh 2kh}, \quad (15)$$

522 where a is the wave amplitude, ω is wave frequency.

523 According to Eq. (15), we can see that the solution is a quadratic function of the ka number. In the present
524 study, the wavelength is constant at $\lambda = 1.8\text{m}$ and the wave height is varied in order to achieve the desired
525 range of ka numbers. Fig. 18 shows the numerical results of drift velocity for the square plate normalized by
526 the wave celerity C as a function of ka number, together with the experimental results of both the present
527 study for the same square plate and Huang et al. (2011) for the square plate of length 20cm and thickness
528 4.5cm. The drift velocity obtained by the Stokes wave theory is also included in the figure for clearer
529 demonstration. Both the numerical and experimental results are slightly larger than the theoretical results as
530 shown in Fig. 18 while they are generally in good agreement.

531
532
533 Fig. 18 Numerical result of drift velocity for the square plate and comparison with the experimental results of both the
534 present study and Huang et al. (2011)

535

536 5.6 Effect of thickness

537

538 The present experimental data has shown that the floe thickness b has a dramatic effect on floe motions,
539 especially in the heave direction. Fig. 19 shows the numerical and experimental results of heave RAO for the
540 square plate with two different thicknesses, $b = 5\text{cm}$ and $b = 7.5\text{cm}$. With increasing of λ/L_c , the heave RAO
541 in both the numerical and experimental results seems to approach the value of 1. The floe with larger
542 thickness has a larger heave response. The experimental results of the square plate with larger thickness also
543 demonstrate that a heave resonance appears, although it is not very obvious. The numerical results seem to
544 follow the same trend as the experimental data, but underestimate the heave RAO, as seen before. The
545 square plate with thickness larger than 7.5cm is not further investigated in the experiment, as the aim of the
546 experiment is to study the motion of sea ice floes with small thicknesses.

547

548

549 Fig. 19 Numerical and experimental heave RAOs for the square plate with two different thicknesses, $b = 5\text{cm}$ and $b =$
550 7.5cm

551

552 As discussed before, the cube has shown an obvious heave resonance at about $\lambda/L_c = 8$. To further
553 investigate this more numerical tests are run for a square plate of length 30cm with various thicknesses
554 ranging from 5cm to 30cm , allowing for the systematic analysis of the effect of thickness as it changes
555 gradually from a square plate to a cube. Fig. 20 shows the numerical result of heave response of those square
556 plates with various floe thicknesses b . We can see from the figure that when the thickness $b \geq 15\text{cm}$ or the
557 relative thickness $b/L_c \geq 0.5$, the heave RAO shows an obvious resonance, and with the thickness increasing,
558 the heave resonance turns to be more and more significant.

559

560

561 Fig. 20 Numerical result of heave response of square plates with variable floe thicknesses b

562

563 6. Conclusion

564

565 A series of physical model tests are conducted to study response of small ice floes in regular water waves.
566 Since this experiment addresses the research gap in the small ice floe kinematics, a numerical simulation of
567 the same problem is necessary to validate the experimental results. Additionally, due to the high demand for
568 resources and time consuming nature of the experiment, finding a reliable numerical tool is vital for the
569 problem of small ice floes in water waves. To achieve this purpose, the linear analysis based on the potential
570 flow model and the CFD simulation based on the viscous flow model are adopted and compared with the
571 experimental data. Many distinct characteristics associated with kinematics of small ice floes in waves are
572 identified in both the numerical and experimental studies.

573 The relative wavelength λ/L_c is found to have dramatic effect on the heave and surge RAOs. The heave
574 resonance occurs for the cube at approximately the relative wavelength $\lambda/L_c = 8$, whereas for the square plate
575 only an increasing trend is observed in the heave response. The present numerical simulation reveals that the
576 heave RAO increases with the floe thickness, and the heave resonance appears at the relative thickness b/L_c
577 ≥ 0.5 . The square and triangle plates with the same thickness b show minimal difference in the heave and
578 surge motions. In the vertical direction the maximum upward and downward velocities are approximately the
579 same. However, in the horizontal direction the maximum forward velocity is larger than the backward
580 velocity and the difference causes the drift displacement. Both the vertical relative velocity V_y/V_p and the
581 ratio of the forward and backward velocities in the horizontal direction V_+/V_- show a resonance at $\lambda/L_c = 8$.
582 No backward velocity is observed when the relative wavelength λ/L_c is relatively small for the square plate;
583 the floe moves forwards all the time. In addition to the comparison with the experimental results, to show the
584 factor which affects the resonance, several additional cases other than that in the experiments are simulated
585 to show the trend of body motions from non-resonance to resonance.

586 The linear results obtained by HydroSTAR[®] seem to overestimate the surge and heave RAOs especially
587 for the cube when the resonance occurs in the range of $\lambda/L_c = 6$ to 9, probably because the nature of linear
588 potential flow model adopted in HydroSTAR[®]. The inaccuracy can also be observed for the square plate
589 considered here in the regime where $\lambda/L_c = 2$ to 4. In general, the open source CFD software OpenFOAM[®]
590 can provide much better agreement with the experimental data than the linear analysis. Extensive CFD
591 simulations and comparisons with the experimental data reveal that the numerical results obtained by
592 OpenFOAM[®] are reasonably accurate, except for the underestimation of the heave RAO for the square plate.

593 The comparison shown in this study indicates that the fluid viscosity is an important parameter which cannot
594 be ignored at laboratory scale when investigating the response of small ice floes in water waves.

595

596 **References**

597

598 Arctic Climate Impact Assessment (ACIA) 2004. Impacts of a Warming Arctic. Cambridge University Press.

599 Arunachalam, V. M., Murray, J. J. and Mugeridge, D. B. (1987). Short term motion analysis of icebergs in linear waves.
600 Cold Reg. Sci. Technol., 13, 247-258.

601 Bennetts, L. G. and Williams, T. D. (2015). Water wave transmission by an array of floating discs. Proceedings of the Royal
602 Society of London A: Mathematical, Physical and Engineering Sciences, 471(2173), 20140698.

603 Chen, X. B., Liu, H. X., & Duan, W. Y. (2015). Semi-analytical solutions to wave diffraction of cylindrical structures with a
604 moonpool with a restricted entrance. *Journal of Engineering Mathematics*, 90(1), 51-66.

605 Blevins, R. D. and Plunkett, R. (1980). Formulas for natural frequency and mode shape. *Journal of Applied Mechanics*, 47,
606 461.

607 Ferziger, J. H. and Peric, M. (2012). Computational methods for fluid dynamics. Springer Science & Business Media.

608 Frankenstein, S., Loset, S. and Shen, H. H. (2001). Wave-ice interactions in the Barents sea marginal ice zone. *Journal of Cold
609 Regions Engineering*, 15 (2), 91-102.

610 Grotmaack, R. and Meylan, M. H. (2006). Wave forcing of small floating bodies. *Journal of Waterway, Port, Coastal, and
611 Ocean Engineering*, 132(3), 192-198.

612 Higuera, P., Lara, J. L. and Losada, I. J. (2013a). Realistic wave generation and active wave absorption for Navier–Stokes
613 models: Application to OpenFOAM®. *Coastal Engineering*, 71, 102-118.

614 Higuera, P., Lara, J. L. and Losada, I. J. (2013b). Simulating coastal engineering processes with OpenFOAM®. *Coastal
615 Engineering*, 71, 119-134.

616 Hirt, C. W. and Nichols, B. D. (1981). Volume of fluid (VOF) method for the dynamics of free boundaries. *Journal of
617 computational physics*, 39(1), 201-225.

618 Huang, G., Wing-Keung, A. L. and Huang, Z. (2011). Wave-induced drift of small floating objects in regular waves. *Ocean
619 Eng.*, 38, 712- 718.

620 Huang, G., Huang, Z. H., & Law, A. W. (2016). Analytical Study on Drift of Small Floating Objects under Regular
621 Waves. *Journal of Engineering Mechanics*, 142(6), 06016002.

622 Jacobsen, N. G., Fuhrman, D. R. and Fredsøe, J. (2012). A wave generation toolbox for the open-source CFD library:
623 OpenFoam®. *International Journal for Numerical Methods in Fluids*, 70(9), 1073-1088.

624 Lever, J. H., Attwood, D. and Sen, D. (1988a). Factors affecting the prediction of wave-induced iceberg motion. *Cold Reg. Sci.*
625 *Technol.*, 15, 177-190.

626 Lever, J. H., Reimer, E. and Diemand, D. (1988b). A model study of the wave-induced motion of small icebergs and bergy bits.
627 *J. Offshore Mech. Arct. Eng.*, 110, 101-107.

628 Lever, J. H., Klein, K., Mitchel, D. and Diemand, D. (1991). Wave-induced iceberg motion. *Cold Regions Science and*
629 *Technology*, 20, 11-23.

630 Marchenko, A. V. (1999). The floating behaviour of a small body acted upon by a surface wave. *J. Appl. Math. Mech.* 63(3),
631 471-478.

632 McGovern, D. J. and Bai, W. (2014a). Experimental study on kinematics of sea ice floes in regular waves. *Cold Regions*
633 *Science and Technology*, 103, 15-30.

634 McGovern, D. J. and Bai, W. (2014b). Experimental study of wave-driven impact of sea ice floes on a circular cylinder. *Cold*
635 *Regions Science and Technology*, 108, 36-48.

636 Meylan, M. H. (2002). Wave response of an ice floe of arbitrary geometry. *J. Geophys. Res.*, 107 (C1), 3005.

637 Meylan, M. H., Yiew, L. J., Bennetts, L. G., French, B. J. and Thomas, G. T. (2015 a). Surge motion of an ice floe in waves:
638 comparison of theoretical and experimental models. *Annals Glaciol.*, 56(69), 107-111.

639 Meylan, M. H., Bennetts, L. G., Cavaliere, C., Alberello, A. and Toffoli, A. (2015 b). Experimental and theoretical models of
640 wave-induced flexure of a sea ice floe. *Physics of Fluids*, 27(4), 041704.

641 Meylan, M. H. and Squire, V. A. (1994). The response of ice floes to ocean waves. *J. Geophys. Res.*, 99 (C1), 899-900.

642 Meylan, M. H. and Squire, V. A., (1996). Response of a circular ice floe to ocean waves. *J. Geophys. Res.*, 101 (C4), 8869–
643 8884.

644 Montiel, F., Bennetts, L. G., Squire, V. A., Bonnefoy, F. and Ferrant, P. (2013a). Hydroelastic response of floating elastic disks
645 to regular waves. Part 2: Modal analysis. *J. Fluid Mech.*, 723, 629-652.

646 Montiel, F., Bonnefoy, F., Ferrant, P., Bennetts, L. G., Squire, V. A. and Marsault, P. (2013b). Hydroelastic response of floating
647 elastic disks to regular waves. Part 1: Wave tank experiments. *J. Fluid Mech.*, 723, 604–628.

648 Morgan, G. and Zang, J. (2011). Application of OpenFOAM to coastal and offshore modelling. In: *Proceedings of 26th*
649 *International Workshop of Water Wave and Floating Bodies*, Athens, Greece.

650 Morgan, G., Zang, J., Greaves, D., Heath, A., Whitlow, C. and Young, J. (2010). Using the rasInterFoam CFD model for wave
651 transformation and coastal modelling. In: *Proceedings of 32nd Conference on Coastal Engineering*. Shanghai, China.

652 Rumer, R. R., Crissman, R. D. and Wake, A. (1979). Ice transport in great lakes. *Great Lakes Environmental Research*
653 *Laboratory*, National Oceanic and Atmospheric Administration, US Dept. of Commerce.

654 Schwerdtfeger, P. (1980). Iceberg oscillation and ocean waves. *Ann. Glaciol.*, 1, 63-65.

655 Shen, H. H. and Ackley, S. F. (1991). A one-dimensional model for wave-induced ice-floe collisions. *Annals Glaciol.*, 15, 87-
656 95.

657 Shen, H. H. and Zhong, Y. (2001). *J. Waterway, Port, Coastal, and Ocean Engineering*, 127(6), 343–351.

658 Squire, V. A. (2007). Of ocean waves and sea-ice revisited. *Cold Reg. Sci. Technol.*, 49, 110-133.

659 Squire, V. A., Dugan, J. P., Wadhams, P., Rottier, P. J. and Liu, A. K. (1995). Of ocean waves and sea-ice. *Ann. Rev. of Fluid*
660 *Mech.*, 27, 115-168.

661 Thomson, J. and Rogers, W. E. (2014). Swell and sea in the emerging Arctic Ocean. *Geophysical Research Letters*, 41(9),
662 3136-3140.

663 U.S. Geological Survey (USGS). (2008). Circum-Arctic Resource Appraisal: Estimates of Undiscovered Oil and Gas North of
664 the Arctic Circle. U.S. Geological Survey Fact Sheet 2008-3049.

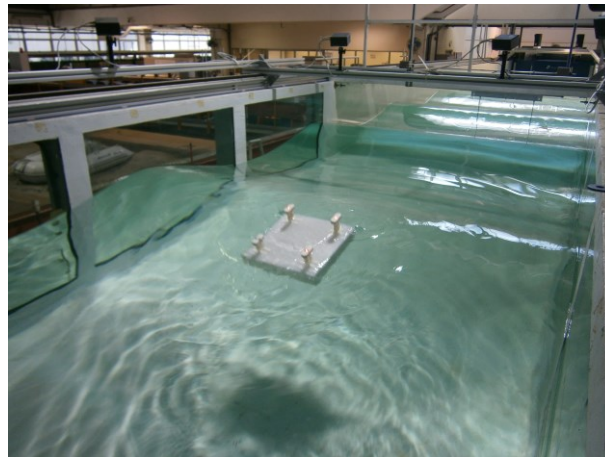
665 Wadhams, P., Kristensen, M. and Orheim, O. (1983). The response of Antarctic icebergs to ocean waves. *Journal of*
666 *Geophysical research*, 88, 6053-6065.

667 Wong, T. T. and Sego, D. C. (1989). Design requirement for ice forces. *Canadian Geotechnical Journal*, 26(4), 524-535.

668

669

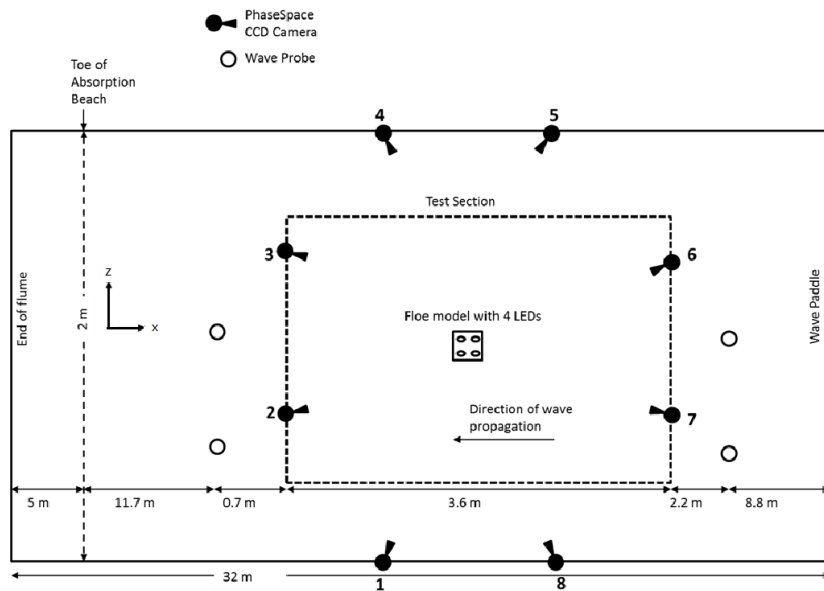
670



(a)

671

672



(b)

673

674

675 Fig. 1 a) Image of a floe model with attached LED lights undergoing testing in regular waves and b) a schematic diagram of
676 the flume.

677

678

679

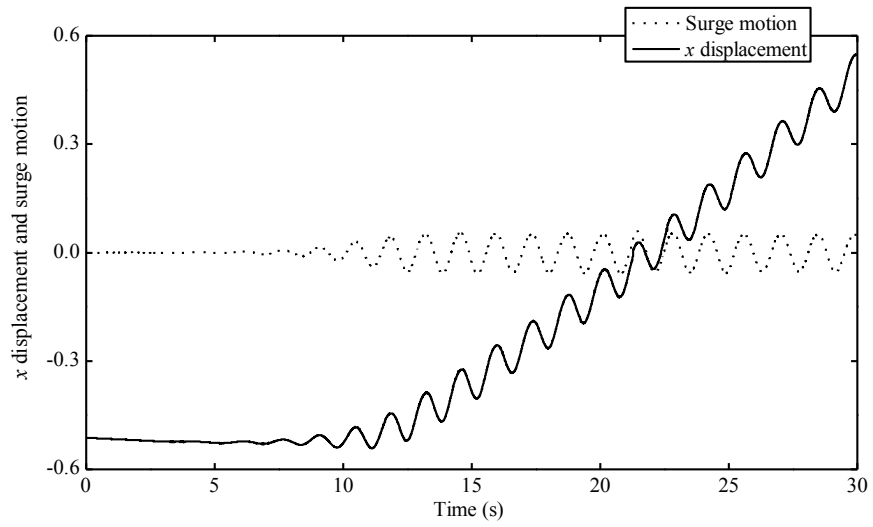
680

681

682

683

684



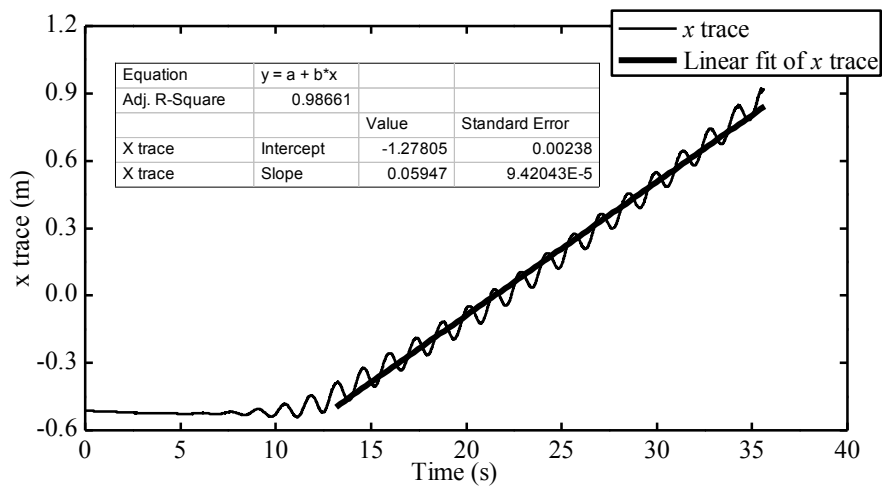
685

686

Fig. 2 An example of x displacement trace in experiment and corresponding surge motion after processing

687

688



689

690

Fig. 3 An illustration of determination of drift velocity V_d using the best-fitting linear line approach.

691

692

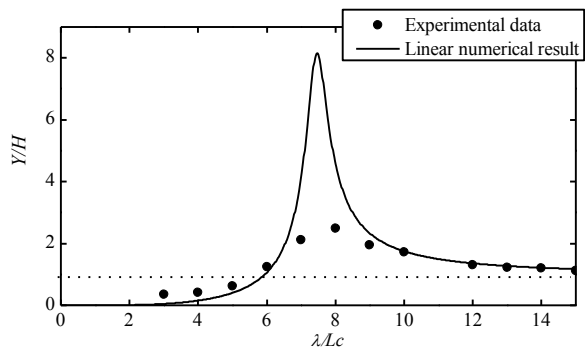
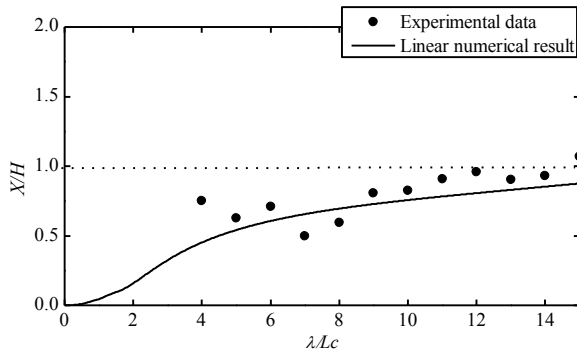
693

694

695

696

697



698

699

(a) Surge

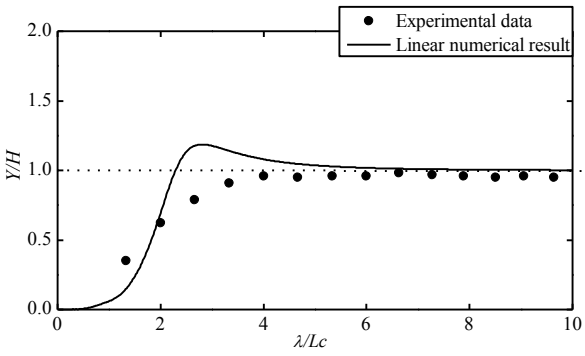
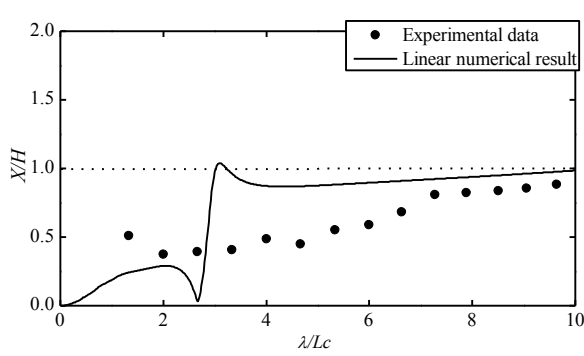
(b) Heave

700

Fig. 4 Comparison of surge (a) and heave (b) RAOs of cube between the linear analysis and experiment

701

702



703

704

(a) Surge

(b) Heave

705

Fig. 5 Comparison of surge (a) and heave (b) RAOs of square plate between the linear analysis and experiment

706

707

708

709

710

711

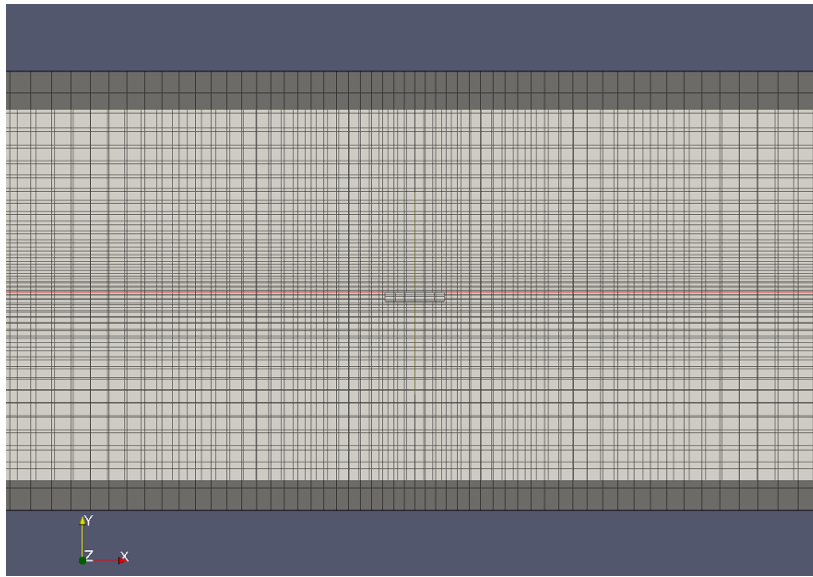
712

713

714

715

716



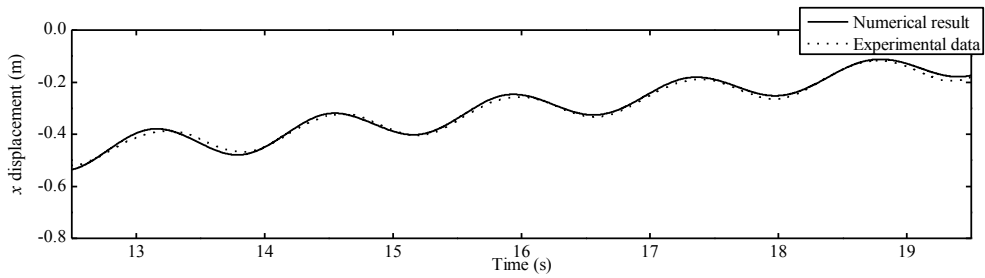
717

718

Fig. 6 The 3D view of an example mesh in OpenFOAM® for ice floe problem

719

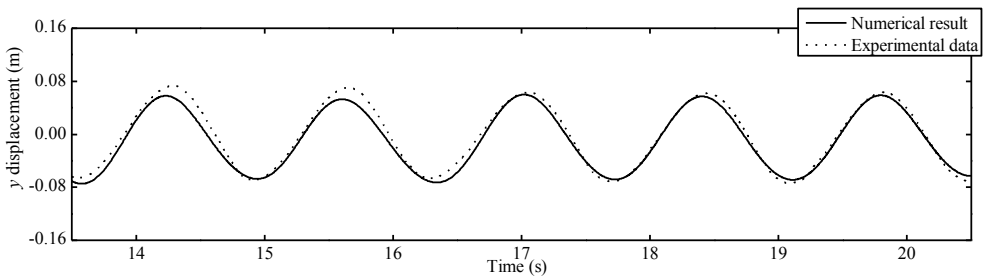
720



721

722

(a) x displacement



723

724

(b) y displacement

725

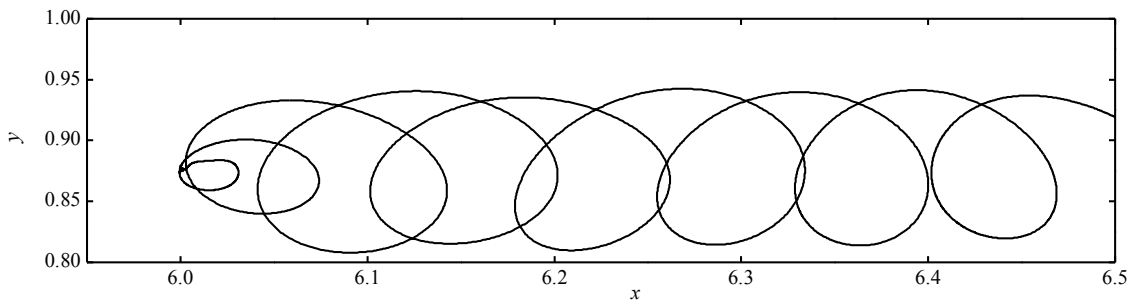
Fig. 7 Numerical and experimental results of time series of x (a) and y (b) displacements for the square plate

726

727

728

729



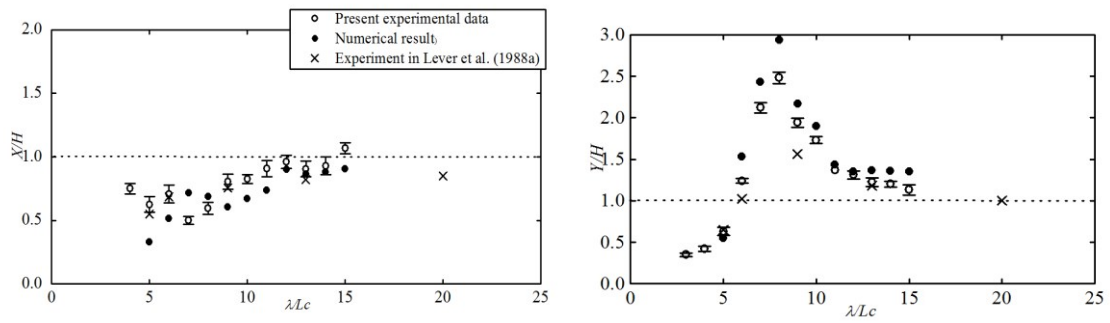
730

731

Fig. 8 Numerical result of trajectory of the square plate in waves

732

733



734

735

(a) Surge

(b) Heave

736

Fig. 9 Comparison of surge (a) and heave (b) RAOs of the cube between the present numerical and experimental results, and the experimental data in Lever et al. (1988a)

737

738

739

740

741

742

743

744

745

746

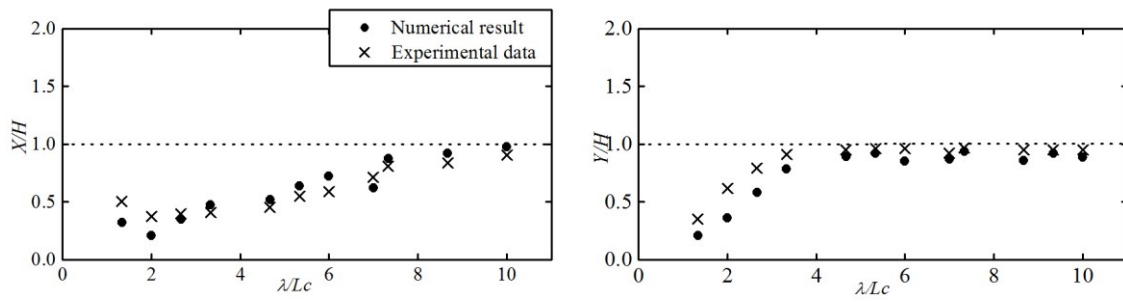
747

748

749

750

751



752

753

(a) Surge

(b) Heave

754

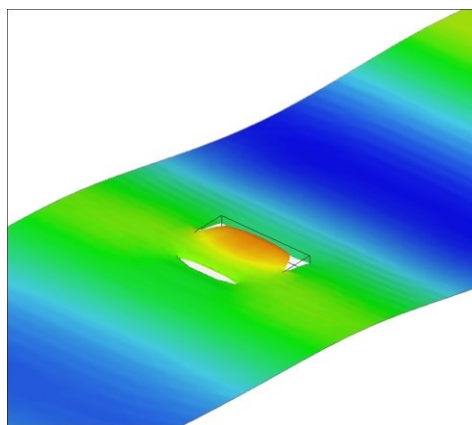
Fig. 10 Comparison of surge (a) and heave (b) RAOs of the square plate between the present numerical and experimental

755

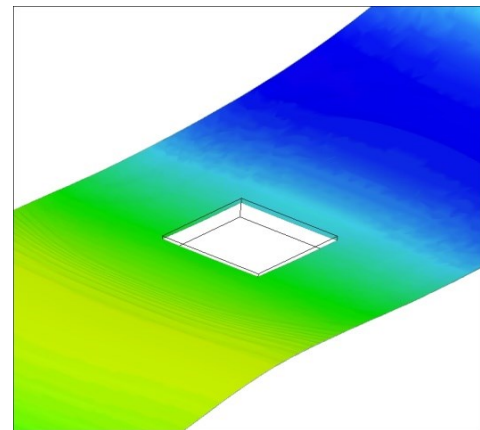
results

756

757



(a) $\lambda/L_c = 4$



(b) $\lambda/L_c = 10$

758

759

Fig. 11 The 3D free surface profile around the square plate for $\lambda/L_c = 4$ (a) with green water and $\lambda/L_c = 10$ (b) without green

760

water

761

762

763

764

765

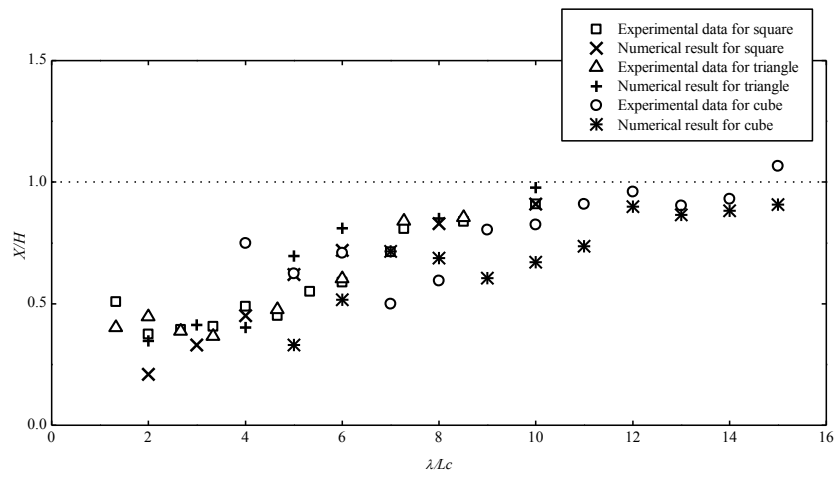
766

767

768

769

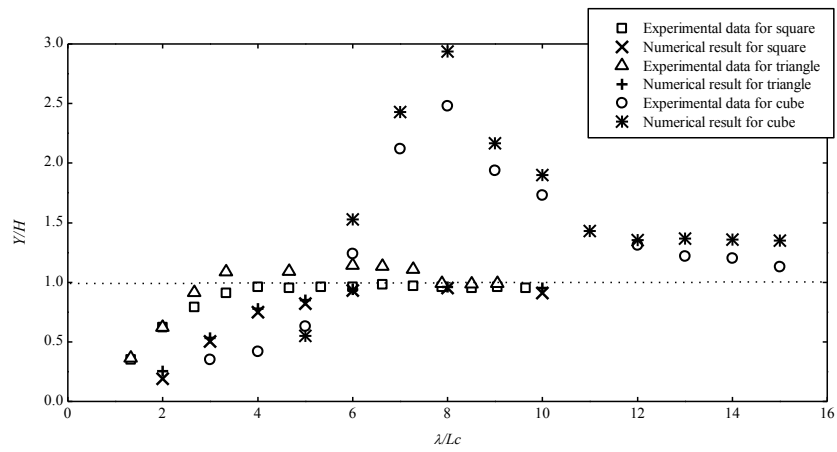
770



771

772

(a) Surge



773

774

(b) Heave

775

Fig. 12 Comparison of surge (a) and heave (b) RAOs of three different body shapes between the present numerical and

776

experimental results

777

778

779

780

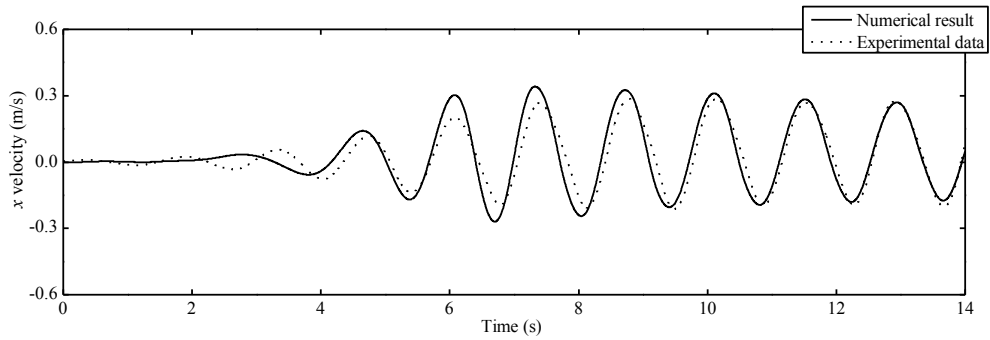
781

782

783

784

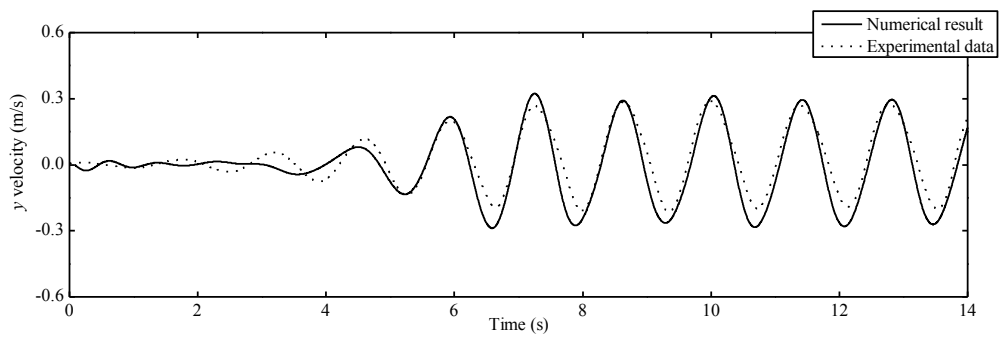
785



786

787

(a) x velocity



788

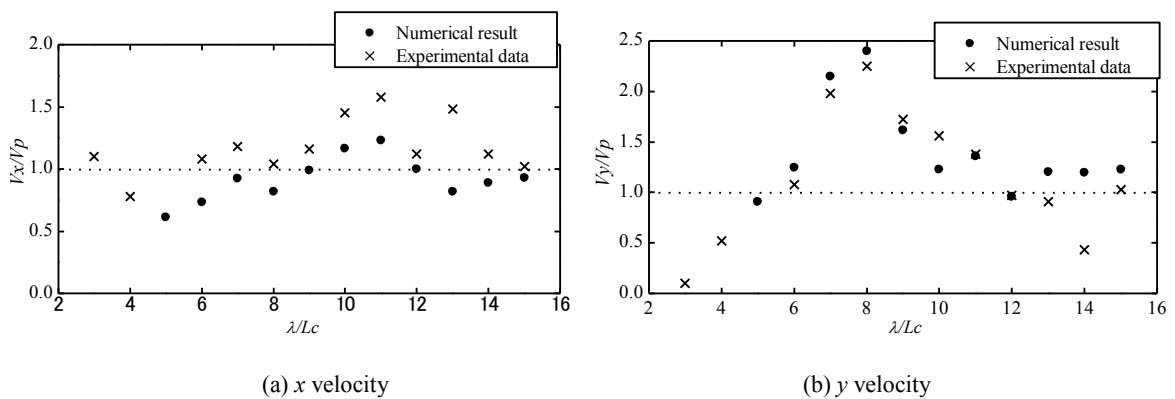
789

(b) y velocity

790 Fig. 13 Time series of x (a) and y (b) velocities obtained by both the numerical simulation and experiment for the square
791 plate with $\lambda = 3\text{m}$ and $H = 0.132\text{m}$

792

793



794

795

(a) x velocity

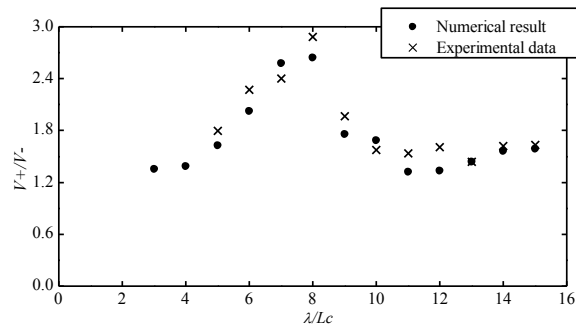
(b) y velocity

796 Fig. 14 Comparison of numerical and experimental results of x (a) and y (b) velocities normalized by the theoretical water
797 particle velocity for the cube

798

799

800



801

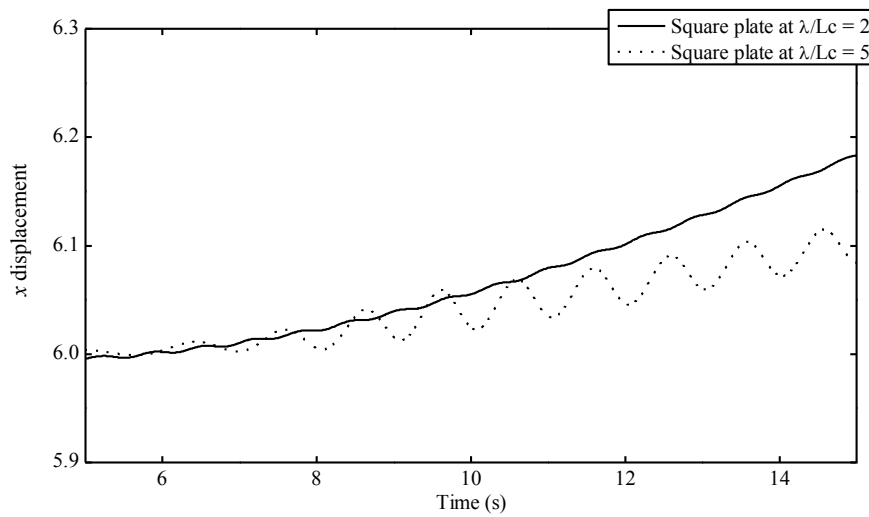
802

Fig. 15 Comparison of numerical and experimental results of the ratio of horizontal positive and negative velocities for the cube as a function of relative wave length

803

804

805



806

807

Fig. 16 Numerical result of displacement in the x direction for the square plate at $\lambda/L_c = 2$ and 5

808

809

810

811

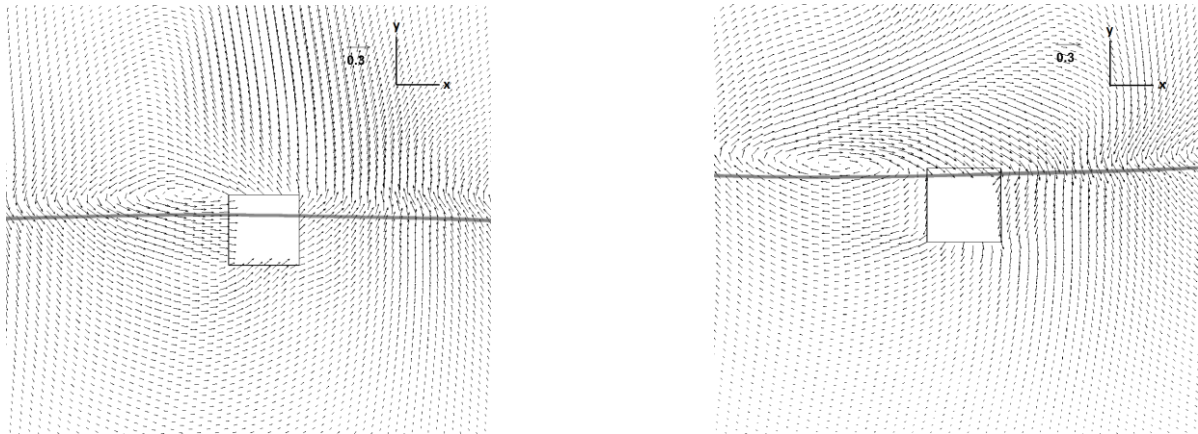
812

813

814

815

816



817

818

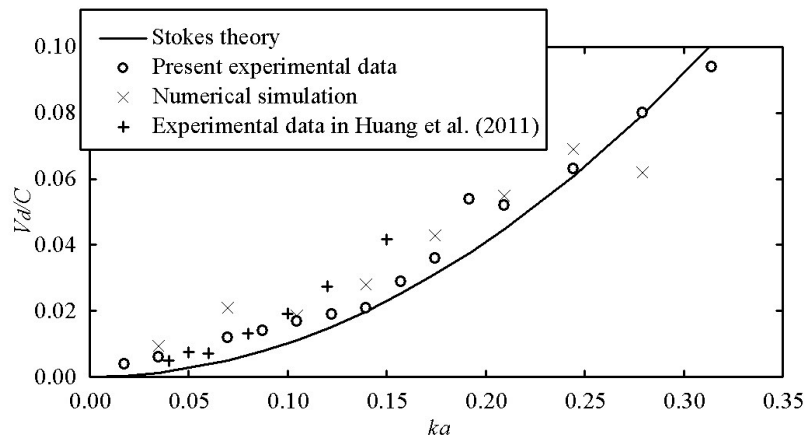
(a) $t = 10.3\text{s}$

(b) $t = 10.9\text{s}$

819 Figure. 17 Velocity field around the cube with $\lambda/L_c = 13$ and $H = 0.052\text{m}$ at two time instants: (a) $t = 10.3\text{s}$ and (b) $t = 10.9\text{s}$

820

821



822

823 Fig. 18 Numerical result of drift velocity for the square plate and comparison with the experimental results of both the
824 present study and Huang et al. (2011)

825

826

827

828

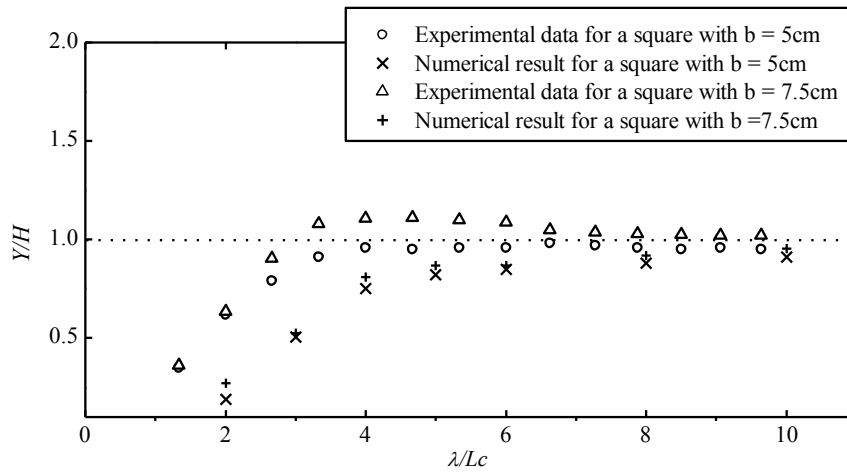
829

830

831

832

833

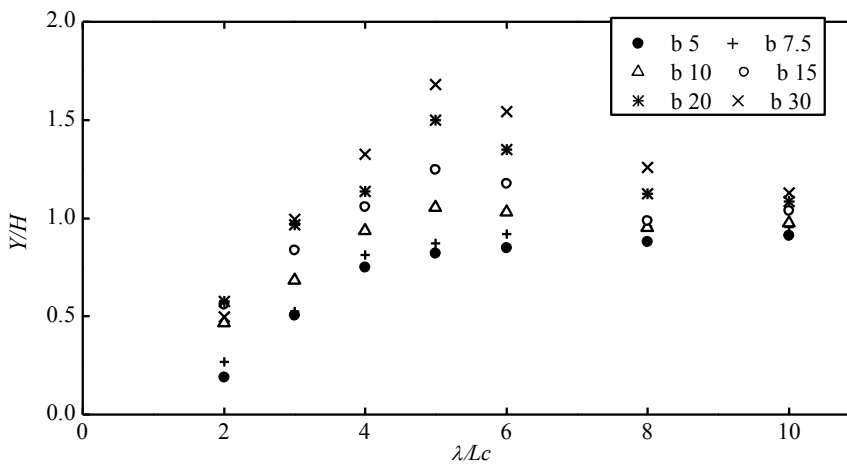


834

835 Fig. 19 Numerical and experimental heave RAOs for the square plate with two different thicknesses, $b = 5\text{cm}$ and $b =$
836 7.5cm

837

838



839

840 Fig. 20 Numerical result of heave response of square plates with variable floe thicknesses b

841

842

843

Table 1 Summary of OpenFOAM® simulations

844

Number of runs	λ (m)	H (m)	H/λ	λ/L_c
Cubic model ($L_c = 20$) with different wavelengths				
11	1 to 3.0	0.02 to 0.06	0.02	5 to 15
Square plate ($L_c = 30$ $b = 5$) with different wavelengths				
12	0.4 to 3.0	0.0176 to 0.132	0.044	1.333 to 10
Triangle plate ($L_c = 30$ $b = 5$) with different wavelengths				
8	0.4 to 2.6	0.0176 to 0.1144	0.044	1.333 to 8.667
Square plate ($L_c = 30$ $b = 5$) with different wave heights				
8	1.8	0.02 to 0.16	0.0111 to 0.0899	6
Square plate ($L_c = 30$ cm) with different thickness $b = 7.5, 10, 15, 20, 30$ cm				
4	0.8	2.0	0.15	0.02

845

846

847